Design and validation of a large-format transition edge sensor array magnetic shielding system for space application

A. Bergen, H. J. van Weers, C. Bruineman, M. M. J. Dhallé, H. J. G. Krooshoop, H. J. M. ter Brake, K. Ravensberg, B. D. Jackson, and C. K. Wafelbakker

Articles you may be interested in

Design of a magnetic shielding system for the time of flight enhanced diagnostics neutron spectrometer at Experimental Advanced Superconducting Tokamak
Review of Scientific Instruments **85**, 11D829 (2014); 10.1063/1.4890536

Optical performance of an ultra-sensitive horn-coupled transition-edge-sensor bolometer with hemispherical backshort in the far infrared
Review of Scientific Instruments **87**, 043103 (2016); 10.1063/1.4945302

Invited Review Article: Single-photon sources and detectors
Review of Scientific Instruments **82**, 071101 (2011); 10.1063/1.3610677

Design of the radiation shielding for the time of flight enhanced diagnostics neutron spectrometer at Experimental Advanced Superconducting Tokamak
Review of Scientific Instruments **85**, 11E115 (2014); 10.1063/1.4891059

Implications of weak-link behavior on the performance of Mo/Au bilayer transition-edge sensors
Journal of Applied Physics **114**, 074513 (2013); 10.1063/1.4818917

A high-performance magnetic shield with large length-to-diameter ratio
Review of Scientific Instruments **83**, 065108 (2012); 10.1063/1.4720943

Nanopositioning Systems   Micropositioning   AFM & SPM   Single molecule imaging

Design and validation of a large-format transition edge sensor array magnetic shielding system for space application

A. Bergen,[1] H. J. van Weers,[2,a)] C. Bruineman,[3] M. M. J. Dhallé,[1] H. J. G. Krooshoop,[1] H. J. M. ter Brake,[1] K. Ravensberg,[2] B. D. Jackson,[2] and C. K. Wafelbakker[4]

[1]*University of Twente, Enschede, The Netherlands*
[2]*SRON Netherlands Institute for Space Research, Sorbonnelaan 2, 3584CA Utrecht, The Netherlands*
[3]*Scientec Engineering, Zuiderzee 23, 1271EP Huizen, The Netherlands*
[4]*DrCKWManagement & Development, Meander 379, 1181 WN Amstelveen, The Netherlands*

The paper describes the development and the experimental validation of a cryogenic magnetic shielding system for transition edge sensor based space detector arrays. The system consists of an outer mu-metal shield and an inner superconducting niobium shield. First, a basic comparison is made between thin-walled mu-metal and superconducting shields, giving an off-axis expression for the field inside a cup-shaped superconductor as a function of the transverse external field. Starting from these preliminary analytical considerations, the design of an adequate and realistic shielding configuration for future space flight applications (either X-IFU [D. Barret *et al.*, e-print arXiv:1308.6784 [astro-ph.IM] (2013)] or SAFARI [B. Jackson *et al.*, IEEE Trans. Terahertz Sci. Technol. **2**, 12 (2012)]) is described in more detail. The numerical design and verification tools (static and dynamic finite element method (FEM) models) are discussed together with their required input, i.e., the magnetic-field dependent permeability data. Next, the actual manufacturing of the shields is described, including a method to create a superconducting joint between the two superconducting shield elements that avoid flux penetration through the seam. The final part of the paper presents the experimental verification of the model predictions and the validation of the shield's performance. The shields were cooled through the superconducting transition temperature of niobium in zero applied magnetic field (<10 nT) or in a DC field with magnitude ~100 μT, applied either along the system's symmetry axis or perpendicular to it. After cool-down, DC trapped flux profiles were measured along the shield axis with a flux-gate magnetometer and the attenuation of externally applied AC fields (100 μT, 0.1 Hz, both axial and transverse) was verified along this axis with superconducting quantum interference device magnetometers. The system's measured on-axis shielding factor is greater than 10^6, well exceeding the requirement of the envisaged missions. Following field-cooling in an axial field of 85 μT, the residual internal DC field normal to the detector plane is less than 1 μT. The trapped field patterns are compared to the predictions of the dynamic FEM model, which describes them well in the region where the internal field exceeds 6 μT. *Published by AIP Publishing.* [http://dx.doi.org/10.1063/1.4962157]

I. INTRODUCTION

SRON, the Netherlands Institute for Space Research, is developing a focal plane assembly (FPA) for future missions that require large-format arrays of transition edge sensors (TES) operating at 50 mK. These detectors are developed as micro-calorimeter arrays for X-ray photon detection, such as for X-IFU (X-ray Integral Field Unit) on Athena[1] and as bolometer arrays for the detection of infrared radiation, as proposed for the SAFARI[2] instrument onboard SPICA (space infrared telescope for cosmology and astrophysics). Frequency domain multiplexing (FDM)[3] is used to read out large TES arrays (3840 sensors for X-IFU) with minimal dissipation in the instrumentation and thermal conduction through the wiring. In the current design the detector array, including wiring fan-out, requires a hexagonal wafer of about ⌀100 mm. The FDM high-Q lithographic resonator circuits and wiring require a significant additional area of up to 220 cm^2 of silicon, which is also cooled to 50 mK and closely packed at the sides of the detector. In total, the 50 mK detector and readout design requires a roughly cylindrical envelope of approximate diameter 100 mm and also a length of $\sim$100 mm. The detector and the FDM readout is enclosed by magnetic shielding in a structural housing. Integrated in this housing are thermally insulating suspensions that separate various temperature levels in the FPA. A more detailed description of the thermal suspension falls outside the scope of this paper, but it is important to keep in mind that apart from the optical entrance and the aperture for feeding out detector wiring, additional openings in the outer shield are necessary to accommodate the suspension of the inner parts.

The performance of TES sensors is inherently susceptible to variations in the magnitude of magnetic fields, since their detection principle is based on the transition between the normal and superconducting states.[4,5] Measurements show that this sensitivity is at least two orders of magnitude larger for fields normal to the detector plane than for fields parallel

---

to it.[5] Hence, optimal performance requires efficient magnetic shielding to provide a low magnetic field environment. Specifically, for the SRON TES arrays, the absolute static magnetic flux density component normal to the detector surface needs to be less than 1 μT during operation. Additionally, the maximum normal magnetic field noise over the detector surface should be less than 200 pT/$\sqrt{Hz}$ for infrared or 20 pT/$\sqrt{Hz}$ for x-ray within the relevant signal bandwidth (1 mHz-30 Hz or 100 Hz-10 kHz, respectively). The main static external magnetic field sources are the earth's field during ground based testing and the proton deflectors used for x-ray application, estimated to be ≤ 100 μT at the FPA. The adiabatic demagnetization refrigerator (ADR) stage induces a field drift estimated at ≤ 2.9 μTh^{-1} and peak fields of 350 μT during regeneration.[6,7] The cooler compressors provide harmonic perturbations, with base excitations estimated at ≤ 5 μT pk @ 30 Hz @ 1 m distance and higher harmonics decaying with 30 dB oct^{-1}.

The operational requirements in terms of magnetic field reduction can then be expressed in terms of a shielding factor S_i, defined as the ratio of the external field B_e to the internal field B_i,[8]

$$S_{ir,z} \equiv B_e/B_{ir,z}. \tag{1}$$

The subscripts "r" and "z" refer to internal field components parallel and normal to the planar detector array, respectively. Note that in some cases, it will be more convenient to use the residual field ratio, defined as $R_{r,z} \equiv \frac{1}{S_{ir,z}}$. A preliminary study at SRON revealed that the magnetic field variations caused by the compressor result in the most stringent requirement, i.e., a shielding factor of $S_{iz} \equiv \frac{B_e}{B_{iz}} = 10^4$ normal to the detector during operation for infrared applications, regardless of the direction of B_e. For x-ray, these values need to be increased by at least an order of magnitude due to the increased dynamic range requirements and to the inherent properties of the TiAu TES bilayer used for this application. In both types of application, the shielding factor for internal fields parallel to the detector plane, S_{ir}, can be 100 times lower. The key requirements imposed by the Athena and SPICA missions are summarized in Table I.

Of course, the shield design should also be physically compatible with the application. All openings in a magnetic shield reduce its effectiveness. The dominant opening in the

FPA is the optical entrance. Its size should be compatible with the dimensions of the incident beam, as described by the ratio between focal length and effective aperture, the f-number. In the case of X-IFU, the f-number is 4, based on a focal length of 12 m and a primary mirror of 3 m. For SAFARI, the f-number is 7. The last optical element at 100 mm from the detector restricts the size of the magnetic shielding in this case. To minimize microphonic noise, the inner shield should be mounted at 50 mK so that relative motion between the detector and the shield, caused by compliance of the thermal suspension, is avoided. To enable space operation, it is also of the utmost importance that the total mass and volume of the shielding system are minimized. The payload needs to be kept as small as possible, to meet the space limitations for the instrument but also to minimize cooling requirements. Since the total cooling system of the FPA consists of multiple cooler stages, each of them limited in efficiency, a small heat load increase at the coldest stage has a large impact at higher temperature levels. This minimization process is described in Sec. II, with the large optical entrance opening in the shields as an additional boundary condition.

The paper is laid out as follows. The design process of the shielding system and its construction is described in Section II. In Subsection II A, straight-forward analytical shield models are discussed that allow a comparison of the relative merits of high-permeability shields with those of superconducting solutions. Based on these findings, a hybrid design is selected and optimized in more detail using the numerical modeling tools described in II B. Subsection II C presents the resulting design together with its predicted shielding behavior. In II D, the physical realization of the shielding system is discussed. Section III reports on the experimental validation of the shielding system and compares its measured performance with the model results from II C. The measurement protocols and instrumentation are described in III A, while Subsection III B presents AC shielding and DC trapped flux data for a wide range of external field configurations and cooling conditions, measured both for the actual hybrid shielding system and for the isolated superconducting inner component. The main findings of this work are discussed in Section IV and summarized in the conclusions Section V.

TABLE I. Magnetic shield design requirements used in this work, based on working assumptions within X-IFU and SAFARI.

| Requirement or parameter	X-IFU Athena	SAFARI SPICA	Comments
Shielded volume	$\varnothing$100 mm $\times$ 100 mm	$\varnothing$100 mm $\times$ 100 mm	
Maximum static (DC) magnetic flux density B_{iz} normal to detector	1 μT	1 μT	
Signal bandwidth	100 Hz-10 kHz	1 mHz-30 Hz	
Required AC shielding factor S_{iz} over the signal bandwidth	$>10^5$	$>10^4$	Shielding factor for internal field component normal to detector surface.
Required AC shielding factor S_{ir} over the bandwidth	$>10^3$	$>10^2$	Shielding factor for internal field components parallel to detector surface.
Maximum external field B_e	<100 μT	<100 μT	
f-number	4	7	X-IFU: based on a focal length of 12 m and a primary mirror diameter of 3 m.
Detector radius r_{det}	12 mm	14 mm	Radial position of outermost pixels.
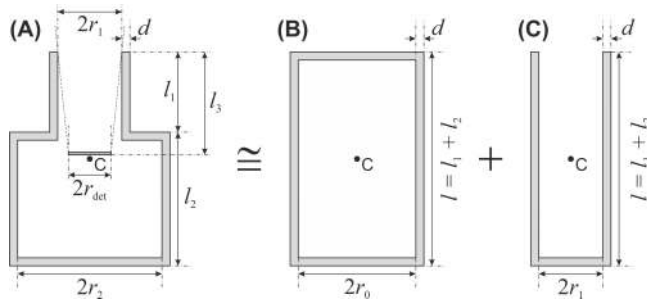
FIG. 1. Schematic representation of a shield geometry with magnetic baffle around the optical entrance. The detector center C is located at $(r, z) = (0, 0)$. To estimate the shielding factor of this geometry, it may be described as a combination of the geometries (b) and (c). (b) accounts for the magnetic flux penetrating through the walls, while (c) is used to describe the effect of the optical entrance.

II. SHIELD DESIGN AND REALIZATION

A. Shield design approach

Several methods can be used to provide the required shielding, ranging from active methods using coils, sensors, and control circuits[8] to passive methods using high-permeability materials,[9–11] superconductors,[12–14] or a combination of these.[15–20] In this work, only passive methods are selected, as these are considered to introduce less complexity and risk of failure during flight.

A basic comparison can be made between a high-permeability and a superconducting shield. In the high-permeability case, even a fully closed shield with a high but finite permeability has a finite shielding factor.[21] When an opening, such as a magnetic baffle, is made in such a shield, two magnetic paths need to be accounted for: flux threading the shield material itself and flux penetrating through the opening. For a superconducting shield, previous reports[22,23] indicate that only the flux penetrating through the opening determines the shielding factor. In this section, we compare the expected performance of a high-permeability shield (with cylindrical geometry and an opening at the detector surrounded by a magnetic baffle, Fig. 1) with a superconducting one.

We first consider a high-permeability shield with wall thickness d, using a method adopted from Mager.[21] For this purpose two separate shielding factors are determined, one to account for the field penetrating through the optical entrance (S_{op}) and another one for the flux threading the walls (S_w). Once these values are determined, the corresponding fluxes are added to yield the effective shielding (S_{eff}) as $\frac{1}{S_{eff}} = \frac{1}{S_w} + \frac{1}{S_{op}}$. S_w and S_{op} both depend on the direction of the external field. To obtain S_w, the geometry shown in Fig. 1(a) is approximated as a cylinder with closed ends, length $l = l_1 + l_2$ and radius

$r_0 = \frac{l_2}{l} r_2 + \frac{l_1}{l} r_1$, see Fig. 1(b). This approximation for r_0 yields a good correspondence between analytical and finite element method (FEM) modeling approaches.

S_{op} on the other hand is calculated using the analytical solutions for the boundary value problem of a one-sided open cylinder with radius r_1 and length l, as in Fig. 1(c). This calculation assumes an infinite permeability of the wall material, which is equivalent to requiring that all tangential components of B vanish at the walls.[12,21,23]

Table II gives the shielding factors for the two separate flux contributions as derived by Mager[21] for both transverse and axial external fields. μ_r is the relative magnetic permeability of the wall material. Note that shielding is less effective for axial external fields than for transverse ones, by a factor q which depends on the ratio $\frac{l}{r_0}$.

For a high-permeability shield with sufficiently small openings, the effective shielding factor S_{eff} for transverse external fields is limited by S_w and thus proportional to the geometric ratio d/r_o and to the permeability μ_r. For shields with a geometric ratio of $\frac{l}{2r_0} > 1$, both axial shielding factors $S_{A,w}$ and $S_{A,op}$ are less effective than the corresponding transverse ones $S_{T,w}$ and $S_{T,op}$. The magnetic baffle needs to be correctly dimensioned to ensure that the effective shielding factor S_{eff} is not limited by the opening. If we apply the dimensions of the Cryoperm shield described below (Section II C, Table III) to this simplified geometry and assume a μ_r value of 20.000, we find $S_{Teff} = 168$ and $S_{Aeff} = 78$.

For a superconducting shield, literature data[22] measured on a cup geometry ($r_0 = r_1 = r_2$) indicate that the internal field only consists of flux penetrating through the opening. In an early stage of the design phase, we measured the on-axis attenuation of an axial field by a straightforward cylindrical Nb tube with openings on both ends. The results, shown in Fig. 2, correspond well to an attenuation factor $R_z \cong 0.29 e^{3.82 \frac{2z-l}{2r_0}}$ with $z = 0$ corresponding to the central mid-plane of the tube. This factor is derived by Vasil'ev *et al.*[22] based only on the effect of the opening.

Note that to maintain the superconducting state, the shield's wall should be thick enough to ensure that the critical current density is not exceeded under maximum external magnetic field conditions.[19] The associated length scale is the London penetration depth λ, which is of the order of 10-100 nm for classical superconductors.[24] The numerical modeling tools developed for the superconducting shield, described in Section II B, allow the current densities occurring in different magnetic environments to be estimated.

From these analytical considerations, it can be concluded that for a high-permeability shield the magnetic field penetrating the walls is likely to limit the maximum achievable

TABLE II. High-permeability shielding factors at the center of the shield configurations shown in Figs. 1(b) (S_w) and 1(c) (S_{op}).[21] The various dimensions are indicated in Fig. 1.

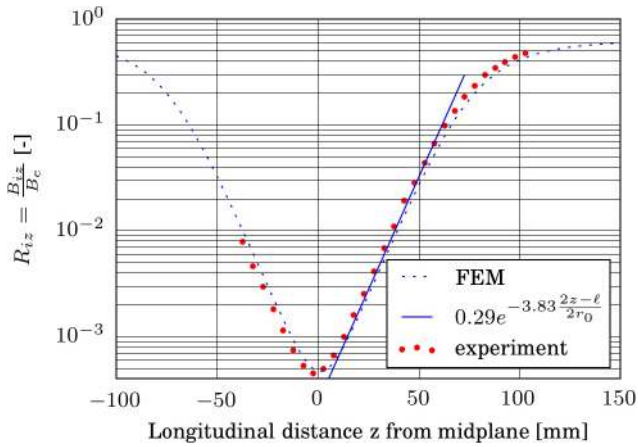| Contribution	Transverse external field	Axial external field
S_w	$S_{T,w} \approx \frac{\mu_r d}{2r_0} + 1$	$S_{A,w} \approx q S_{T,w}$ with $q \approx 1.33 e^{-0.45 \frac{l}{2r_0}}$ for $1 < \frac{l}{2r_0} < 3$
S_{op}	$S_{T,op} \approx 3.0 e^{3.52 \frac{l_3}{r_1}}$	$S_{A,op} \approx \frac{1}{1.3\sqrt{\frac{l}{2r_1}}} e^{2.26 \frac{l_3}{r_1}}$

FIG. 2. Comparison between measurement, FEM model, and analytical approximation of the on-axis attenuation of an axial external field for a superconducting Nb tube. Tube dimensions: inner radius $r = 39$ mm, length $\ell = 140$ mm, and thickness $d = 3$ mm.

shielding factor, while this is not the case for a superconducting shield. A higher shielding factor can thus in principle be realized using a thin-walled superconductor than with a thin walled high-permeability shield of the same size. Based on these findings, the design described in this paper uses a superconducting shield to provide most of the required shielding factor.

On-axis attenuation factors for superconducting cups are given by both Mager[21] and by Claycomb and Miller.[23] However, due to the lateral size of the detector array, the B_z field requirements also hold up to a radial distance r_{det} from the central axis (see Table I). For a transverse external field, the highest internal B_z component over the detector plane occurs off-axis at the detector edge $r = r_{det}$. Using the method described by Vasil'ev *et al.*,[22] the internal B_z component for a transverse external field acting on a cup geometry with length $l = l_1 + l_2$, radius r_0, and $z = 0$ at the bottom of the cup can be approximated as

$$B_z(r, \phi, z) = \frac{B_{z0}(r_0, \ell)}{J_1(y_{11}) \sinh(y_{11})} \times J_1(y_{11} \frac{r}{r_0}) \cos \phi \sinh(y_{11} z - l_3/r_0), \quad (2)$$

with J_1 the Bessel function of the first kind and using $y_{11} \cong 1.8412$. By introducing $\hat{X} = \ell/r_0$ and the following approximations, $\tilde{Q}_{11} \cong 0.229$, $\tilde{I}_1 \cong 0.29$, the normalization field, on-axis at the entrance of the cup, can be expressed as

$$B_{z0}(r_0, \ell) = \frac{y_{11} \tanh(y_{11} \hat{X})}{1 - \frac{1}{y_{11}^2}} \frac{I_1(\hat{X})}{[1 + \tilde{Q}_{11}]}. \quad (3)$$

Although a superconducting shield in principle offers higher shielding factors than a high-permeability one, its effectiveness can be compromised by external magnetic fields that become "frozen in" during cool-down.[25] Mechanical,[26] thermal,[27,28] and electromagnetic[29] methods have been employed or proposed to reduce this effect, but they all rely on additional instrumentation, rendering them less straightforward for space-based application. In the design proposed and tested in this paper, similar to Xu and Hamilton[30] and to Hishi *et al.*,[19] an outer high-permeability shield is therefore included to

reduce the external fields on the superconducting shield during its transition. The aim is to minimize the amount of static magnetic flux trapped in the superconducting shield.[31,32] Such trapped flux may have two sources. In multiply connected structures such as this one, flux threading apertures will be "conserved" during cool-down into the Meissner state. In the remainder of the paper, this effect is referred to as "geometric flux trapping." Additionally, for type II superconductors, flux threading the material itself can also become trapped in the form of flux quanta that are generated while the material passes the Abrikosov vortex state.[33] This will be called "microscopic flux trapping." Nevertheless, for the present design the type II material Nb was chosen, partly because its intrinsic properties (critical temperature and field) and partly because of the technological know-how that is available from its use in accelerator cavities (for details, see Section II C). For the high-permeability shield, Cryoperm 10 was selected,[34] a Ni-Fe alloy that is optimized for use at cryogenic temperatures.

B. Modeling

Several FEM models were used (all implemented in the COMSOL Multiphysics[35] environment), during the design phase of the shield assembly as well as for the interpretation of the experimental data that are presented in Section III. For the high-permeability Cryoperm shield, static models were used with a non-constant relative permeability $\mu_r(B)$. To determine this permeability, the BH curves of welded cylindrically rolled shields were measured using an AC method with two winding sets and an analog integrator, conform to ASTM International standard test method A773/A773M-01. The excitation frequency used was 200 mHz. For a sample with $r_0 = 25$ mm, $l = 100$ mm, and $d = 1$ mm, BH curves were taken both at ambient temperature and at 4 K.

The $\mu_r(H)$ curves, shown in Fig. 3, were derived from these data using the relation $B = \mu_r \mu_0 H$. For the shielding system discussed in this paper, the maximum H field in the Cryoperm 10 is of the order of 1 Am^{-1} for a maximum external field of 100 μT. From theory[36] the magnetization curve in this region typically follows the relation $\frac{dB}{dH} = \mu_{r0}\mu_0 + \nu H$, with μ_{r0} the initial permeability and ν a constant. Extrapolation of the data to H = 0 Am^{-1} yields $\mu_{r0} \approx 1.45 \times 10^4$. It is noteworthy that the often-quoted maximum permeability of this type of shielding materials (of the order of 10^5) is of little relevance here. Initially observed variations between curves of the same sample were traced back to unintentional mechanical stress variations in the sample caused by its fixture. As an example, the $\mu_r(H)$ curve for the same sample is included under a mechanical stress of approximately 2 MPa. The data shown in Fig. 3 were used in the FEM models during further optimization of the shield design. Shielding factors are calculated using a standard implementation of Ampere's law $\nabla \times [(\mu_0 \mu_r)^{-1} \nabla \times A] = J^e$, with the magnetic vector potential defined as $B = \nabla \times A$ and J^e an externally generated current density.

For the superconducting shield, two types of FEM model were used. Shielding factors were computed with the same implementation of Ampere's law, in which the superconductor was omitted from the computational domain and replaced
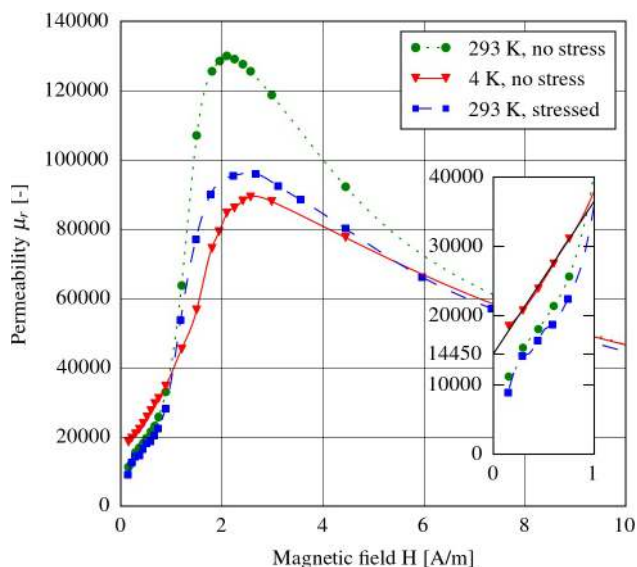
FIG. 3. The magnetic permeability μ_r of a Cryoperm 10 welded cylinder measured at room temperature (green circles and blue squares) and at 4 K (red triangles). For one of the room temperature experiments (blue squares), a mechanical stress level of approximately 2 MPa was applied to the sample. The inset shows the region below H = 1 A m^{-1} and the extrapolation used to determine the initial permeability μ_{r0}.

by a "magnetic insulation" boundary condition $(\nabla \times A)_n = 0$. This simple approach was verified for a simple tube geometry and matches well with the data; see Fig. 2. Note that this type of model does not take into account the history of the superconductor and therefore will be referred to as "static." In Section III below, it will be compared to the zero-field cooled (ZFC) experiments. To model a more realistic field-cooled (FC) scenario, the macroscopic effect of flux trapping during cool-down through the superconducting transition is accounted for by using an unconstrained-H formulation model.[37,38] In this "dynamic" type of modeling approach, the superconductor is approximated as a classical ideal conductor. In the transient study, the electrical resistivity of the superconductor is varied in time. Initially an arbitrary high value of $\rho = 10^2 \ \Omega m$ is used to approximate Nb in the normal state, see Figs. 5(a) and 5(b). With this resistivity value, the external field is ramped up to the level applied during transition. Next the resistivity of the Nb domain is lowered to a value approaching zero without field changes, which mimics cool-down of the Nb to its superconducting state. At this point, the superconductor is modeled as an ideal conductor. Finally, the external field is reduced to zero, inducing currents inside the superconductor that maintain trapped flux both through the walls (microscopic trapping) and through the central opening (geometric trapping), see Figs. 5(c) and 5(d).

C. Detailed design

Cryoperm is available only in sheet metal form, ranging in thickness from 0.5 to 2 mm in steps of 0.5 mm. It can be welded and machined, followed by a heat treatment to optimize the permeability at cryogenic temperatures. Since the detector unit needs to be placed inside, the Cryoperm shield has to be split into a top and bottom part, with the separation
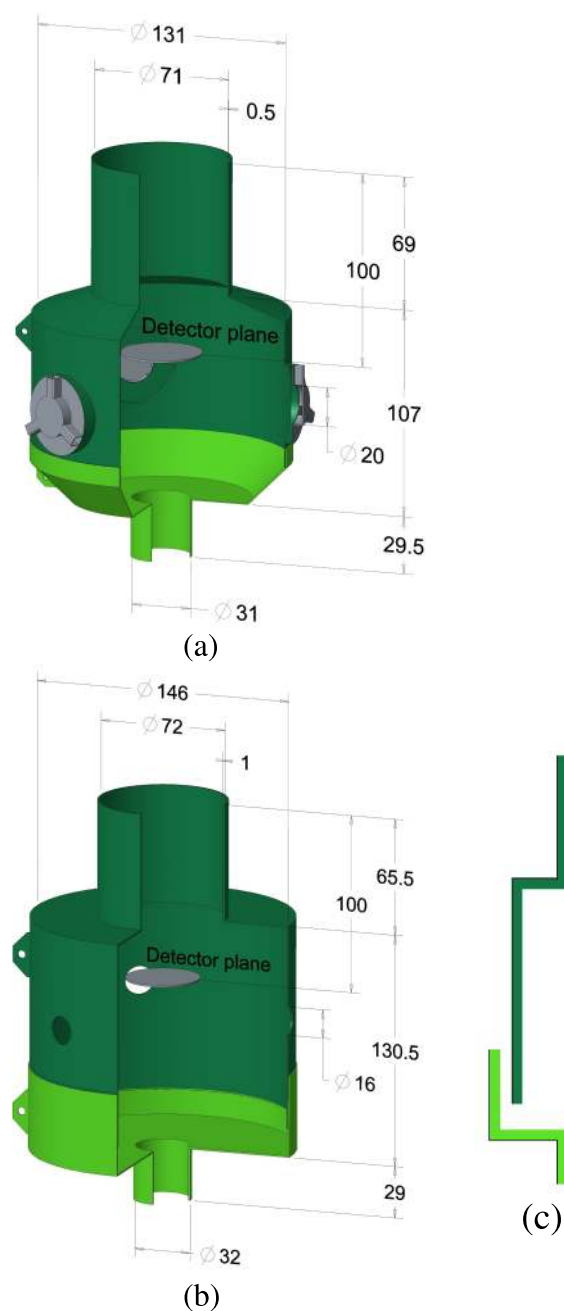

(a)

(b)

(c)

FIG. 4. Design iterations of the Cryoperm shield. (a) Initial design, gap 0.2, overlap 10 mm, holes for inner structure supports closed with separate covers. (b) Final design, gap 0.2, overlap 30 mm, with small openings for inner structure supports. (c) Schematic view of overlap between two Cryoperm parts. "Gap" refers to the difference between the inner radius of the bottom part and the outer radius of the top one.

at the largest diameter. An additional opening at the bottom of the shield allows thermal links from the cooler and electrical interconnects to enter. The initial design, shown in Fig. 4(a), incorporated separate elements to shield the radial holes for the detector support structure. For this design, the FEM analysis described above yielded $S_z = 39$ as on-axis shielding factor at the detector for axial external fields. In several design iterations the gap dimensions, diameter, and length were varied and optimized. The final design, shown in Fig. 4(b), is based on 1 mm wall thickness and an overlap of 30 mm, with a gap dimensioned to less than 0.2 mm per side. After this

optimization, the FEM prediction for the Cryoperm shielding factor at the detector was $S_{iz} = 66$. In Section II A, a shielding factor $S_{iz} = 78$ was estimated analytically for the simplified geometry. This was based on an assumed value for μ_r of 20.000. Using the same constant μ_r-value in a FEM model of the final geometry with and without gap, we find $S_{iz} = 62$ and 68, respectively, which is reasonably in agreement. The hole diameter for the detector support structure was minimized such that the separate covers could be omitted without a significant reduction in performance.

Several low-[12–14,39] and high-temperature[40–44] superconducting materials have successfully been employed for shielding purposes. For the superconducting shield in this paper, niobium was selected based on the following properties. First, its relatively high transition temperature ensures that the shield will remain superconducting even while the instrument coolers are recycled. During recycling, the temperature of the magnetic shields will rise to about 4-6 K, depending on the regeneration procedure. If this would drive the superconducting shield normal, a different static field might be trapped after each cooldown, which is undesirable. Furthermore Nb has a relatively high critical magnetic field, which increases the maximum allowable external field. Finally, its hardness can be influenced during fabrication, which enables the application of a s.c. joint technique as described in Subsection II D. Just like the Cryoperm, the Nb shield also needs to have a parting line for insertion of the detector module. For this purpose, following input from Heraeus GmbH based on their experience with linear accelerators,[45] a conflat-like sealing technique was implemented to create a superconducting interface between top and bottom parts. This seal combines oxygen-hardened knife-edged Nb flanges with a softer sealing ring of annealed pure Nb. During assembly, the knife edges cut through the Nb oxide layers that are present on all parts, thus ensuring a superconducting connection.

The dimensions used for both shields are given in Table III. They are determined based on the SAFARI requirements for which the optical entrance l_3 is limited to 100 mm, $r_{det} = 14$ mm, and f = 7. The radius r_2 has been slightly reduced for both shields, to fit the shielding in a non-metallic Dewar during magnetic testing. The shielding factor for an axial and transverse external field is shown in Fig. 5.

D. Shielding realization

Based on the modeling results described above, the fabrication method of the Cryoperm shield was altered to create a closer fit between the top and bottom parts than would

TABLE III. Main dimensions of the inner Nb and outer Cryoperm 10 shield. The various parameters are defined in Fig. 1.

Dimension [mm]	Nb	Cryoperm
r_1	25	35
r_2	46.5	72
ℓ_1	80	65.5
ℓ_2	75	130
ℓ_3	100	100
d	0.5	1.0

be feasible with rolling and welding. For this purpose, the mating surfaces on both parts were machined on a lathe with dedicated tooling (Fig. 6, top). This tightened the gap to less than 0.2 mm per side. After machining, the parts were sent back to the supplier for the final heat treatment[46] to optimize the permeability at cryogenic temperatures. The detailed heat treatment schedule is proprietary knowledge of the supplier, but it starts with 5 h at 1150 °C in a dry H_2 atmosphere followed by a holding time of 2 h at a lower temperature and finally a well-defined cooling rate down to about 200 °C. A similar treatment is discussed in Ref. 46.

The Nb shield assembly was fabricated by Heraeus GmbH from high-purity Nb with 200 ppm Ta content (Fig. 6, bottom). Using spin forming, a thin-walled geometry with two smoothly connected cylindrical sections (⌀50 mm × 80 mm and ⌀93 mm × 75 mm) was realized from a single sheet without additional welding. The residual resistance ratio (RRR value) of the initial bulk material was measured to be 392, after spin forming of the rolled sheet this reduced to an RRR value between 166 and 226. The oxygen-hardened flanges with a hardness of 240 DPH were then laser welded to the spin-formed thin parts.

III. SHIELD VALIDATION

A. Experimental details

The performance of the hybrid shield assembly was experimentally verified in a magnetically shielded room of $2.4 \times 3 \times 4$ m^3. The background field in the center of the room was measured to be less than 10 nT. Two mutually orthogonal coil sets were used to apply a homogeneous field in the axial or the transverse direction to the hybrid shield assembly. The axially applied field was measured to vary less than 1% over a volume of $280 \times 280 \times 200$ mm^3 around the center of the shield assembly, the transverse one over a volume of $165 \times 230 \times 230$ mm^3.

In order to gauge the possible effect of flux frozen-in during the superconducting transition of the Nb (Subsection II A), the hybrid and the isolated Nb shield were both tested in two distinct cool-down situations, as indicated in Fig. 7 and in Table IV. The figure schematically shows the magnetic "phase diagram" of a type II superconductor. The shields were either zero-field cooled (ZFC) following the trajectory depicted by the red arrows, or field cooled (FC), as shown by the blue arrows. In both the ZFC and FC experiments, the residual field ratio $R = S^{-1}$ was measured along the z-axis (the axis of rotational symmetry) after the shields were cooled and, in the FC case, after removal of the external field. For these R(z) measurements, an AC (triangular shaped) bipolar field sequence was applied either transverse or axially. The frequency was 0.1 Hz and the amplitude 85 μT in the axial direction and 100 μT in the transverse one. Note that the first critical field (H_{c1}) of Nb is approximately 0.15 T, so even in spite of the large demagnetizing effects involved, the Nb should remain well inside the Meissner state.[47] This point is further discussed in Section III B 1. The x, y, and z components of the flux density along the z-axis were measured with a three-axis superconducting quantum interference device
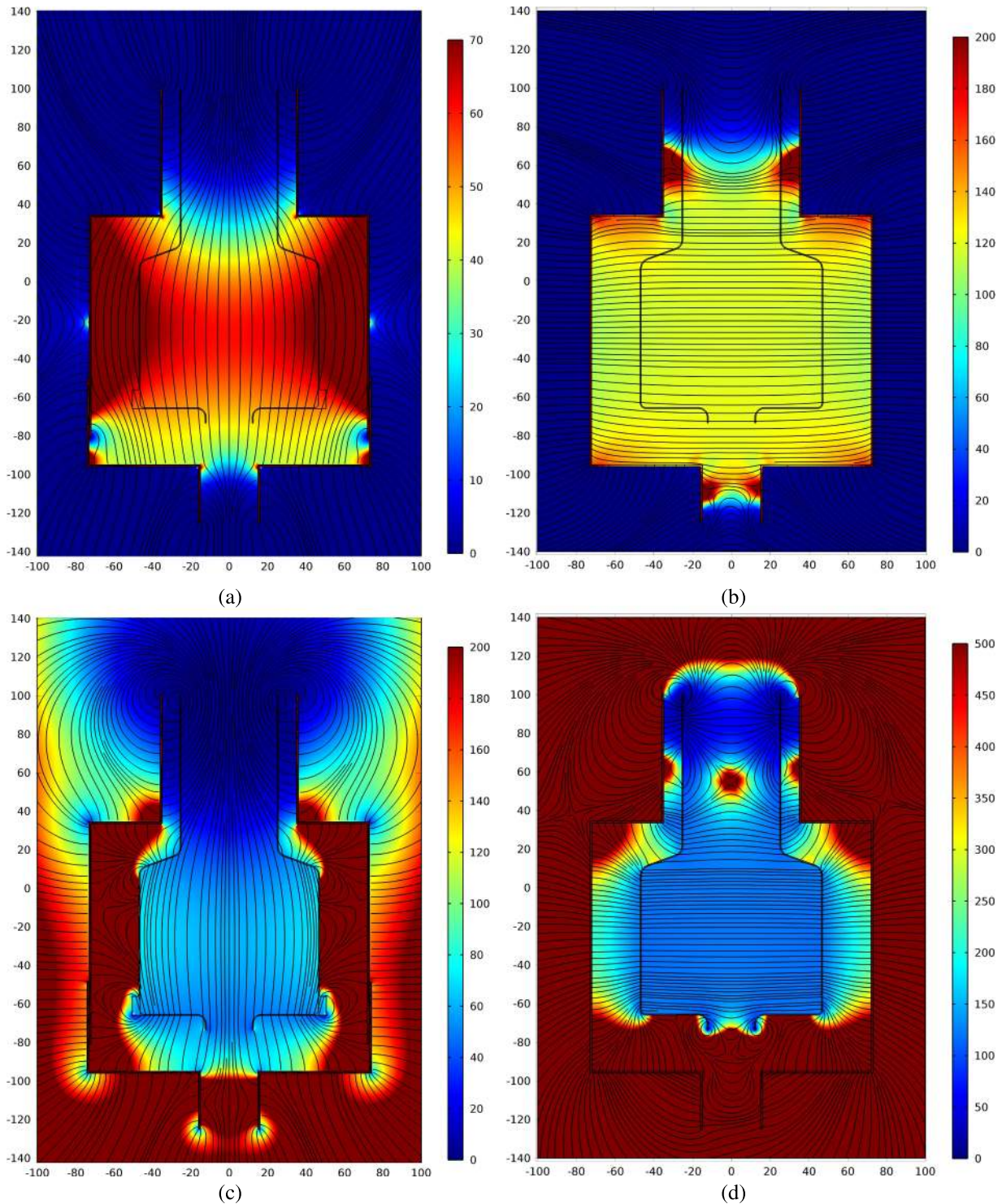
FIG. 5. Dynamic (unconstrained-H) FEM modeling of flux trapping in axial and transverse external fields. The color scales indicate the shielding factor $S_{ir,z} = \frac{B_e}{B_{ir,z}}$, using the overall magnitude of B_i. In Section III of the paper, these FEM predictions are compared to experimental data along the axis of rotational symmetry. (a) Axial external field above T_c. (b) Transverse external field above T_c. At this temperature, only the Cryoperm shield is active. (c) Axial field-cooled, below T_c and after removal of the external field. Note that in this situation, the initially applied field is used to determine S_{iz}. The model shows that most of the remanent flux is trapped microscopically. Only a small fraction of the field at the detector stems from geometrical flux trapping. (d) Transverse field-cooled, below T_c and with external source removed. Also here the initial applied field is used to determine S_{ir}. Microscopic flux trapping through the Nb walls occurs over the complete shield. For comparison with experiments, the residual on-axis fields corresponding to situations (c) and (d) are also plotted in Figs. 14 and 15, respectively, (a) Axial, $T > T_c$, $B_{ext} = 85\ \mu$T. (b) Transverse, $T > T_c$, $B_{ext} = 100\ \mu$T. (c) Axial, $T < T_c$, $B_{ext} = 0\ \mu$T. (d) Transverse, $T < T_c$, $B_{ext} = 0\ \mu$T.

(the Supracon AG "3Dgreen" SQUID, with a sensitivity of 1.6 $pT/\sqrt{Hz}$) and the relevant component was plotted against the applied field. The slope of these graphs was used as a measure for the residual field ratio R and is compared to the

results of the static FEM models described in Subsections II B and II C.

Note that the chosen measurement frequency of 0.1 Hz is at the lower end of the required bandwidth in the envisaged
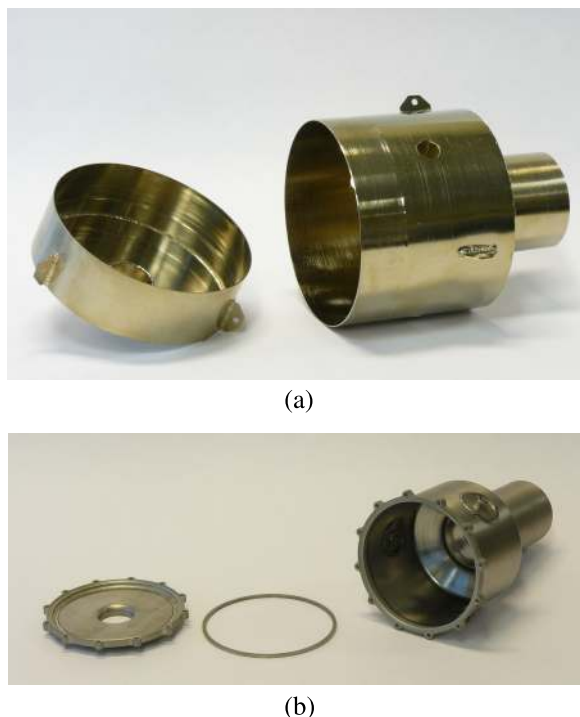
(a)

(b)

FIG. 6. The shielding hardware prior to final assembly. (a) Cryoperm hardware after heat treatment; the turned sections have slightly deviating surface finish. (b) Nb shielding assembly bottom, seal ring, and top part.

SAFARI and X-IFU instruments (up to 30 Hz an up to 10 kHz, respectively, see Table I). This experimental frequency was chosen to avoid eddy-current effects arising from metal structures in the cooler and the rest of the measurement setup. However, at the supplier, the ambient-temperature AC attenuation of the Cryoperm shield was also measured in the frequency range from 1 Hz up to 10 kHz. As suggested by Mager,[21] initially the shielding factor S increases with
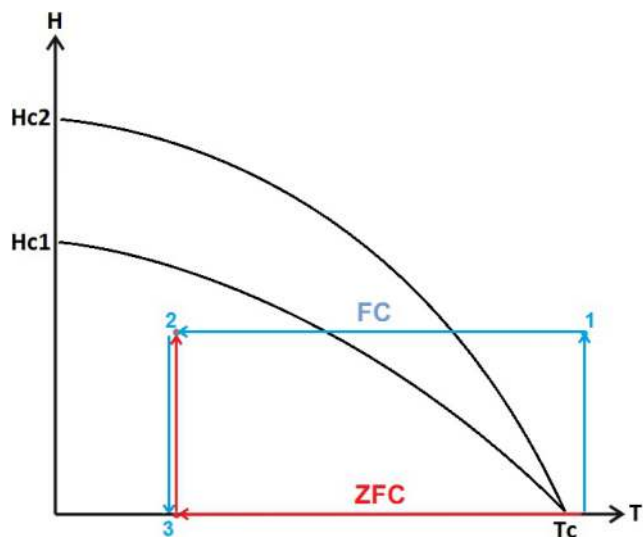
FIG. 7. Schematic diagram illustrating the difference between the zero field cooled (ZFC, red line) and field cooled (FC, blue lines) procedures. With both procedures, the response of the shields to AC fields was measured around point 3. For the FC situation, also the DC magnetic field was measured before cool-down (in point 1), after cool-down (point 2) and after turning off the "cool-down" magnetic field (point 3).

frequency to reach a maximum at about 100 Hz. For higher frequencies up to 10 kHz, the shielding factor did not reduce below the values measured at 1 Hz. For the superconducting shield, we did not verify the frequency dependence. However, in the time-dependent Ginzburg-Landau formalism, deviations of the superconducting order parameters from its equilibrium value are expected to relax with a time constant $<10^{-12}$ s,[41,48] i.e., with frequencies that are several orders of magnitude higher than those relevant in this work.

In the case of the FC procedure, additional data were collected to gauge the importance of DC trapped flux. The absolute magnetic field was measured before and after cool-down and after the static field was removed, as indicated in Fig. 7 by points 1, 2, and 3. Due to the inherent uncertainty in the locking state of SQUID magnetometers, they can only straightforwardly measure magnetic field variations, making them less suited for absolute field experiments. Therefore, the absolute field profiles were measured with a fluxgate sensor (Bartington MagF) with a range up to 200 μT and a resolution of 1 nT. This device may be operated between liquid helium and ambient temperature. The absolute field profiles will be compared to the dynamic unconstrained-H FEM predictions described in Subsection II C.

Lastly, a temperature sensor placed on the bottom of the Nb shield showed that (during the filling of the helium bath cryostat) the superconductor passed through its transition with a cooling rate of the order of 1 K/s. In between successive measurement series on just the Nb shield, liquid He was siphoned out of the cryostat and the shield was heated up above Tc with a resistive heater, in order to wipe out any magnetic history. To start the measurements in a well-defined condition, also the Cryoperm was demagnetized between each measurement on the hybrid shield assembly. For this demagnetization process, the whole assembly was heated to room temperature and removed from the cryostat. A copper wire was threaded through the top aperture of the shielding system, fed down its center line, and extracted at the bottom opening. Repeating this procedure by feeding the wire back into the top, five turns were established which were supplied with a sinusoidal current with an amplitude corresponding to a field of >100 A/m and then slowly brought down to zero. This demagnetization procedure of the Cryoperm was carried out inside the magnetically shielded room.

B. Results

In this subsection, the measured data are presented and compared to the predictions of the static and dynamic models described in Subsection II C. In view of the relatively large number of experiments performed on different shield configurations, an overview of figures together with corresponding shield and measurement conditions is provided for convenience in Table IV.

1. Zero-field cooled

After the ZFC procedure, the residual field ratio R for external AC fields was measured for both the isolated Nb shield and for the combined hybrid shield, as shown in Figs. 8

TABLE IV. Overview of the experimental data presented in the paper. The column "Shield" refers to the shielding system (either only the superconducting Nb or the combined Nb/Cryoperm shield); "Cooling" refers to the DC field applied during cool-down through the superconducting transition ("zero" means <10 nT in all directions; "axial" and "transverse" to ~100 μT applied either along the shields symmetry axis or perpendicular to it); "Trapped flux" refers to on-axis measurements of the DC trapped flux density (either its axial or its transverse component); and "Shielding" refers to measurements of the attenuation of an externally applied AC field (~100 μT, 0.1 Hz). All data are collected along the rotational symmetry axis of the shielding system.

Shield and cooling procedure		Data		
Shield	Cooling	DC trapped flux	AC shielding	
Nb	ZFC	...	Axial and transverse	Fig. 8
Combined	ZFC	...	Axial and transverse	Fig. 9
Nb	Axial	Axial	...	Fig. 10
Nb	Transverse	Transverse	...	Fig. 11
Nb	Axial and transverse	...	Axial and transverse	Fig. 12
Combined	Axial	Axial	...	Fig. 14
Combined	Transverse	Transverse	...	Fig. 15
Combined	Axial and transverse	...	Axial and transverse	Fig. 16

and 9. For the Nb shield, the experimental data correspond well with the straightforward static model predictions that account for the superconductor as a "magnetic insulation" boundary (Subsection II B). In the model calculations, the discontinuity in the tangential component of the flux density can be translated into a sheet current density which turns out to be maximal (~10^3 A/m) at the edge of the optical entrance. Combined with a London penetration depth of ~50 nm for Nb,[24] this yields a current density of ~10^{10} A/m^2, i.e., well below its estimated depairing current density ~$3 \cdot 10^{12}$ A/m^2 associated with the Meissner state.[24] Note also how the agreement between the data and the static model predictions suggests that the conflat sealing technique (Section II C) indeed establishes a superconducting connection between the top and bottom parts of the Nb shield. To illustrate this, static model predictions assuming a non-superconducting gap of 50 and 100 μm width (dashed and dotted lines, respectively) between both shield parts have also been added to Fig. 8. Clearly, the flux leakage associated with such a "hairline" gap would have led to a significantly lower shielding factor relative to the ones actually observed.

In the case of the hybrid shield shown in Fig. 9, there is a small offset that is most likely caused by the connection between the two Cryoperm pieces. Nevertheless, as aimed for in the design, the hybrid shield does reach an axial shielding factor at the detector plane well above $S = 10^6$ for axial AC fields and slightly below $S = 10^4$ for transverse ones. Both values meet the requirements imposed by the envisaged space missions (Table I).

2. Field cooled

During the FC procedure, the absolute DC magnetic field was determined at the temperature/external field points 1, 2,
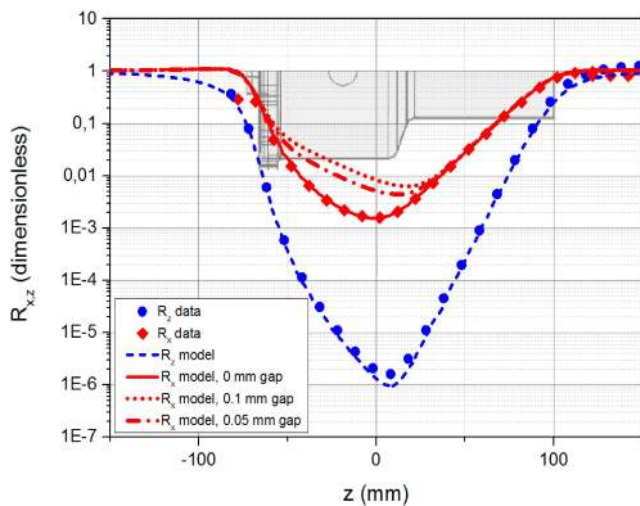

FIG. 8. Measured AC residual field ratio $R_{x,z} = \frac{B_{x,z}}{B_e}$ measured along the z-axis for the isolated Nb shield (shaded inset) after cooling in zero field (ZFC), in the case of an axially (blue circles, $B_e = 85$ μT) or transverse (red diamonds, $B_e = 100$ μT) applied field. The dots represent the data, the lines the predictions of the static FEM calculations. The dotted and dashed red lines represent FEM predictions for a shield with a small but finite gap between the top and bottom part (Section II C), the solid line is modelled without gap.
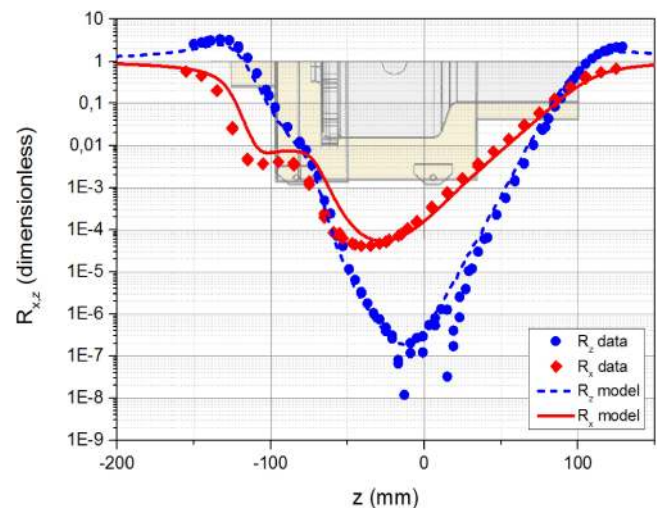

FIG. 9. Measured AC residual field ratio $R_{x,z}$ along the z-axis for the combined hybrid shield (shaded inset) after ZFC in an axial (blue circles, $B_e = 85$ μT) or transverse (red diamonds, $B_e = 100$ μT) applied DC field. The dots represent the data, the lines the predictions of static model.
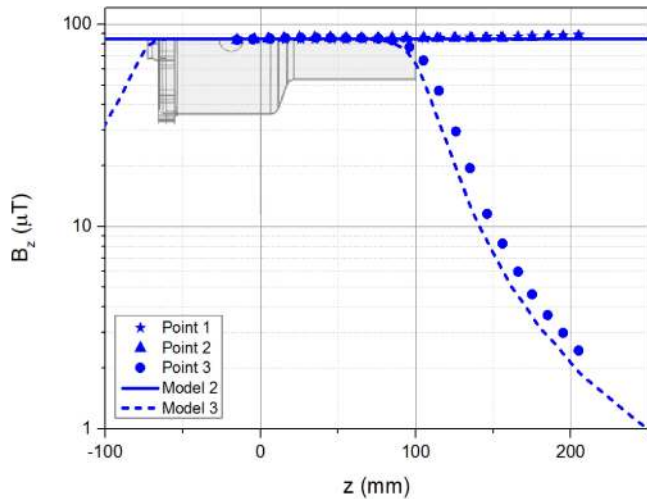
FIG. 10. Absolute z-component of the DC magnetic field measured along the axis of rotational symmetry of the isolated Nb shield (shaded inset) during and after cooling in an axial field of 85 μT (FC). The stars indicate the measured field before cool-down (point 1 of Fig. 7), the triangles after cool-down (point 2), and the dots after cool-down and removal of the external magnetic field (point 3). The solid line is the dynamic model prediction at point 2, the dashed line the prediction of the same model at point 3.

FIG. 12. The AC residual field ratio $R_{x,z} = \frac{B_{x,z}}{B_e}$ for an axially (blue symbols, $B_e = 85$ μT) and transverse (red symbols, $B_e = 100$ μT) applied field measured along the z-axis of the isolated Nb shield (shaded inset) after a FC procedure in either an axial (blue circles and red diamonds) or a transverse (blue triangles and red squares) DC field. The lines correspond to the same static model predictions as the ones shown earlier in Fig. 8.

and 3 indicated in Fig. 7. Figs. 10 and 11 show the measured field along the z-axis after cool-down of the Nb shield in an axial or a transverse applied magnetic field of 85 μT and 100 μT, respectively. In these figures, the stars correspond to the field at point 1 (in-field, above T_c), the triangles to point 2 (in-field, below T_c), and the dots to point 3 (zero external field, below T_c). Included as lines are the predictions of the dynamic model at points 2 and 3, determined with the unconstrained-H method as described in Subsection II B. The data confirm that the Nb shield freezes-in the magnetic field. In a transverse field, geometric flux trapping in principle only occurs due to small misalignment errors (estimated to be <3°) and ensuing

axial field components (estimated <5 μT). The substantial magnitude of the remanent field inside the shield after the transverse FC procedure (~100 μT, Fig. 11) therefore clearly confirms that microscopic flux trapping also plays a major role.

The AC residual field ratio R of the Nb shield was also determined separately after a FC procedure and is depicted in Fig. 12. Unlike the ZFC data presented in Fig. 8, the experimental data for the transverse FC scenario clearly deviate from the static model predictions in the region ranging from −50 mm below to +30 mm above the focal plane assembly. From the ZFC data, it was concluded that the conflat seal performs well, so that this deviation is unlikely to be associated with the link between both shield parts. In this region, the SQUID response plotted against the applied AC field also displayed a clear hysteretic signature, as shown in Fig. 13. Such hysteretic magnetization in type II superconductors is typically associated with the motion of quantized flux vortices in the presence of strong pinning centers.[49] This reinforces the observation that significant microscopic flux trapping occurs, which clearly also influences the AC shielding capacity of the Nb shield when it is not enclosed within the high-permeability shield.

The outer Cryoperm shield was designed to reduce external fields acting on the inner superconducting one and thus to minimize the amount of trapped flux. DC magnetic field measurements at the different stages of the FC procedure were also performed on the hybrid design and are shown in Fig. 14 for cool-down in an axial field and in Fig. 15 for a transverse field. Comparison with the corresponding data measured with only the Nb shield (Figs. 10 and 11) immediately shows that the Cryoperm indeed strongly reduces the amount of trapped flux. The measured data at high field values correspond well to the dynamic model, especially considering that this model simply assumes the superconductor to behave as an ideal conductor. However, in both FC orientations remaining
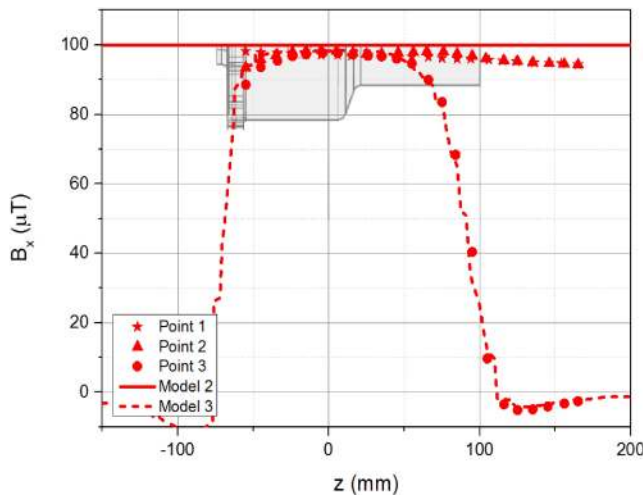

FIG. 11. Absolute x-component of the DC magnetic field measured along the axis of the isolated Nb shield (shaded inset) during and after a transverse FC procedure (x is the direction of the 100 μT applied field). The stars indicate the measurements before cool-down (point 1 of Fig. 7), the triangles after cool-down (point 2), and the dots after removing the external magnetic field (point 3). The solid line is the dynamic model prediction at point 2, the dashed line at point 3.
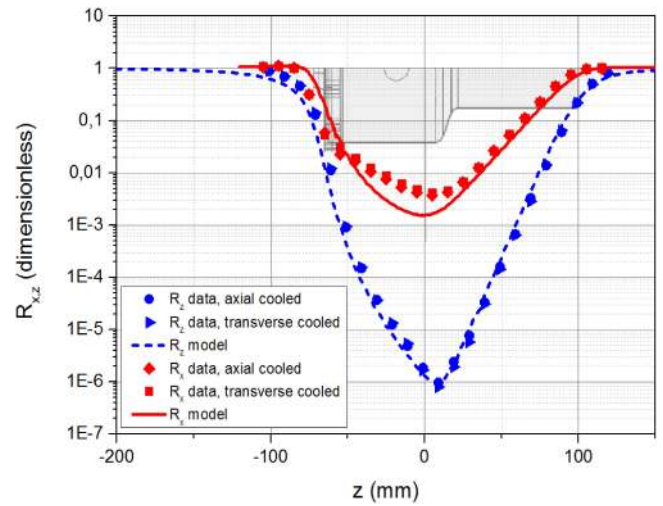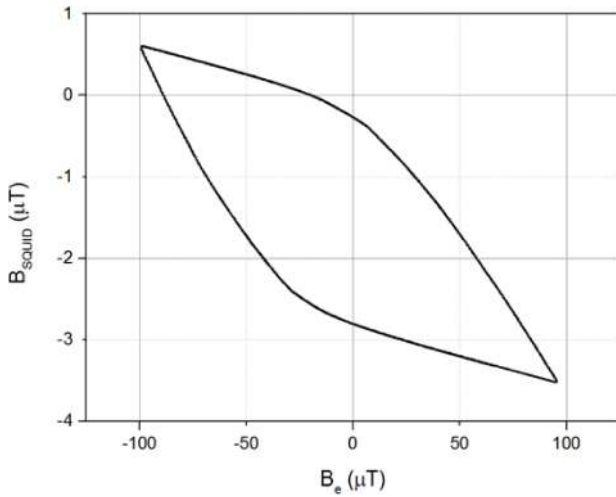
FIG. 13. SQUID Bx signal corresponding to the data point at z = −35 mm in Fig. 12 (the on-axis AC residual field ratio measured in the transverse FC Nb shield by itself), plotted against transverse applied AC magnetic field. Similar hysteretic curves are measured after field cooling in the whole region −50 mm ≤ z ≤ 30 mm, where the measured AC residual field ratio deviates from the static model predictions (see Fig. 12). Note that the SQUID is only sensitive to field variations, so that the vertical axis has an arbitrary offset.

deviations between data and model on the smallest field scale (inset in Fig. 15) illustrate that further model refinements are needed to describe the detailed flux behavior at the detector plane during cool-down, e.g., by explicitly taking the non-linear current density-electric field relation of the superconductor into account.[20,44,50] Nevertheless, comparing the AC residual field ratios R measured inside the hybrid shield under FC conditions (shown in Fig. 16) with those obtained after a ZFC procedure (Fig. 9) reveals that the influence of the remaining trapped flux is minimized and that both scenarios follow the static model to good agreement.
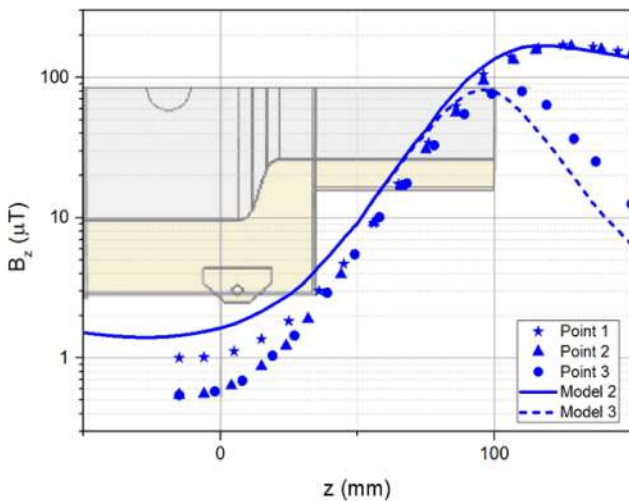

FIG. 14. The absolute z-component of the DC magnetic field measured along the axis of hybrid shield (shaded inset) cooled in an axial field of 85 μT. The stars indicate the data before cool-down (point 1 of Fig. 7), the triangles after cool-down (point 2), and the dots after cool-down and removal of the magnetic field (point 3). The solid line represents the dynamic model prediction at point 2, the dotted line is that at point 3 (i.e., the situation illustrated earlier in Fig. 5(c)).
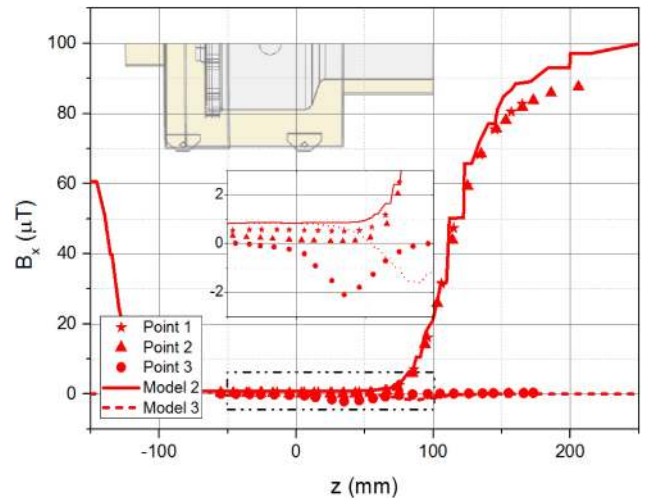

FIG. 15. The absolute x-component of the DC magnetic field measured along the axis of the hybrid shield (shaded top inset) that was cooled in a 100 μT transverse field. The stars indicate the data before cool-down (point 1 of Fig. 7), the triangles after cool-down (point 2), and the dots after cool-down and removal of the magnetic field (point 3). The solid line is the dynamic model prediction at point 2 (the steps are artefacts due to the discretization), the dotted line is that at point 3 (i.e., the situation illustrated earlier in Fig. 5(d)). The central inset shows the same data in the region −50 < z < 100 mm with more detail around B = 0.

A close comparison between Figs. 15 and 16 appears to reveal a discrepancy. Removal of the 100 μT DC external transverse field during the FC procedure (i.e., the transition from point 2 to point 3 in Fig. 15) leads to a change of ∼2 μT in the internal field at z = 35 mm. Subsequent measurements of the transverse AC residual field ratio in the same region (Fig. 16) yield a value of $R = 4 \cdot 10^{-3}$, i.e., five times lower than suggested by the data in Fig. 15. It should be noted, however, that the measured flux density changes in Fig. 15 are likely to be related to the rearrangement of pinned microscopic vortices trapped during cool-down (see also Figs. 5(b) and 5(d)), whereas in Fig. 16 "new" flux lines enter the shield from the outside. The reasonable agreement with the static
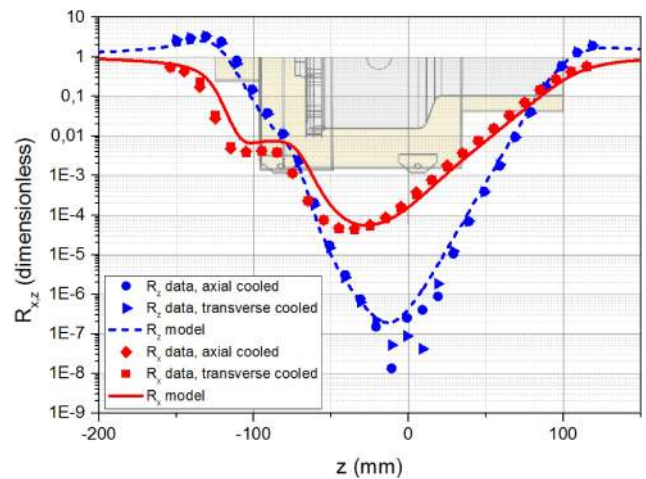

FIG. 16. The AC residual field ratio $R_{x,z} = \frac{B_{x,z}}{B_e}$ for an axially (blue symbols) and transverse (red symbols) applied field measured along the axis of the FC hybrid shield (shaded inset). The circles and diamonds represent the data after cool-down in axial field, the triangles and squares in a transverse field. The lines correspond to the static model predictions.

model prediction (i.e., with the magnetic insulation boundary condition) suggests that in this latter experiment flux "curves in" through the top aperture, similar to the situation shown for the Cryoperm shield in Fig. 5(b).

IV. DISCUSSION

In the center of the FPA, the measured shielding factor for the field component normal to the detector plane is $S_{iz} = 4 \cdot 10^6$ in response to an axially applied field and $S_{ir} = 5 \cdot 10^3$ for transverse applied fields (Fig. 16). Both values exceed the requirements for SAFARI and may also suffice for X-IFU. The measured residual field ratios show good agreement with the static FEM models. Although no experimental off-axis data were collected on the combined shield, the model predicts $S_{iz} > 5 \cdot 10^4$ at $r_{det} = 12$ mm (X-IFU) for the minimum shielding normal to the array and $S_{ir} > 2.5 \cdot 10^4$ at $r_{det} = 14$ mm (SAFARI) for a transverse external field. Confidence in these predictions is strengthened by the good agreement between measured data and model predictions observed on the axis of the shield assembly. Field-cooled measurements demonstrate that the normal field component trapped during transition in a 85 μT axial external field is of the order of 1 μT (Fig. 14). Field-cooling in transverse fields results in an even lower field component normal to the array.

V. CONCLUSION

The performed verification of the on-axis attenuation demonstrates that the combined Cryoperm/Nb shielding system meets the requirements as defined within SAFARI ($S_{iz,measured} = 4 \cdot 10^6 > S_{iz,required} = 10^4$; $S_{ir,measured} = 5 \cdot 10^3 > S_{ir,required} = 10^2$, see Table I). The modeled off-axis shielding does not meet the more stringent requirement of $S_{iz} > 10^5$ imposed by X-IFU over the full array. However, by extending the length l_3 of the magnetic baffles of the niobium and Cryoperm shields to 110 and 130 mm, respectively, while at the same time increasing their diameters according to the f-number, the FEM models predict that also this requirement can be met (yielding $S_{iz,modeled} = 6.5 \cdot 10^5$ at $r_{det} = 12$ mm and increasing towards the center). This illustrates nicely how these relatively straightforward modeling tools allow versatile adaption of designs to meet the requirements of different applications.

Both types of FEM model (using Ampere's law for the static model and the unconstrained-H formulation to describe the dynamic case) have been extensively used during the design and verification process. In the static model, replacing the superconductor with a boundary condition and using the measured $\mu_r(H)$ relation have proven to be a reliable method to predict the achieved attenuation for a combined Cryoperm and Nb shield. Under the relatively fast cooling conditions enforced by He vapor, the macroscopic effect of flux trapping in the Nb shield is reasonably well described with the dynamic model when one approximates the superconductor as an ideal conductor. A new test setup is in preparation in which the same shielding assembly can be conductively cooled at a lower cooling rate, which is more representative for a realistic space cooling system. This will allow verification of the influence of cooling rate on the residual trapped field under field

cooling conditions.[51,52] For this purpose, the unconstrained-H formulation has proven to be a valuable tool to estimate trapped flux effects.

[1]D. Barret, J. W. den Herder, L. Piro, L. Ravera, R. Den Hartog, C. Macculi, X. Barcons, M. Page, S. Paltani, G. Rauw, J. Wilms, M. Ceballos, L. Duband, L. Gottardi, S. Lotti, J. de Plaa, E. Pointecouteau, C. Schmid, H. Akamatsu, D. Bagliani, S. Bandler, M. Barbera, P. Bastia, M. Biasotti, M. Branco, A. Camon, C. Cara, B. Cobo, L. Colasanti, J. L. Costa-Kramer, L. Corcione, W. Doriese, J. M. Duval, L. Fabrega, F. Gatti, M. de Gerone, P. Guttridge, R. Kelley, C. Kilbourne, J. van der Kuur, T. Mineo, K. Mitsuda, L. Natalucci, T. Ohashi, P. Peille, E. Perinati, C. Pigot, G. Pizzigoni, C. Pobes, F. Porter, E. Renotte, J. L. Sauvageot, S. Sciortino, G. Torrioli, L. Valenziano, D. Willingale, C. de Vries, and H. van Weers, e-print arXiv:1308.6784 [astro-ph.IM] (2013).

[2]B. Jackson, P. de Korte, J. van der Kuur, P. Mauskopf, J. Beyer, M. Bruijn, A. Cros, J. Gao, D. Griffin, R. den Hartog, M. Kiviranta, G. de Lange, B. van Leeuwen, C. Macculi, L. Ravera, N. Trappe, H. van Weers, and S. Withington, IEEE Trans. Terahertz Sci. Technol. **2**, 12 (2012).

[3]R. A. Hijmering, R. H. den Hartog, A. J. van der Linden, M. Ridder, M. P. Bruijn, J. van der Kuur, B. J. van Leeuwen, P. van Winden, and B. Jackson, *The 160 TES Bolometer Read-Out Using FDM for SAFARI* (SPIE Conference Proceedings, 2014), Vol. 9153, pp. 91531E–1–91531E–12.

[4]L. Gottardi, H. Akamatsu, M. Bruijn, J.-R. Gao, R. den Hartog, R. Hijmering, H. Hoevers, P. Khosropanah, A. Kozorezov, J. van der Kuur, A. van der Linden, and M. Ridder, J. Low Temp. Phys. **176**, 279 (2014).

[5]R. Hijmering, P. Khosropanah, M. Ridder, J. R. Gao, M. Lindeman, H. Hoevers, J. van der Kuur, L. Gottardi, B. Jackson, R. Huiting, and M. van Litsenburg, IEEE Trans. Appl. Supercond. **23**, 2101505 (2013).

[6]L. Duband, I. Charles, and J.-M. Duval, *Coolers Development for the ATHENA X-IFU Cryogenic Chain* (SPIE Conference Proceedings, 2014), Vol. 9144, pp. 91445W–1–91445W–10.

[7]N. Luchier and L. Duband, in *Cryocoolers 13*, edited by J. Ross and G. Ronald (Springer US, 2005), pp. 561–566.

[8]R. A. S. Celozzi and G. Lovat, *Electromagnetic Shielding* (John Wiley and Sons, Inc, 2008).

[9]J. F. Hoburg, IEEE Trans. Electromagn. Compat. **37**, 574 (1995).

[10]A. Moldovanu, H. Chiriac, C. Ioan, E. Moldovanu, M. Lozovan, and V. Apetrei, Int. J. Appl. Electromagn. Mech. **9**, 421 (1998).

[11]Z. Q. Cui, Z. J. Chen, X. F. Xie, X. Y. Peng, Z. M. Hu, T. F. Du, L. J. Ge, X. Zhang, X. Yuan, Z. W. Xia, L. Q. Hu, G. Q. Zhong, S. Y. Lin, B. N. Wan, T. S. Fan, J. X. Chen, X. Q. Li, and G. H. Zhang, Rev. Sci. Instrum. **85**, 11D829 (2014).

[12]K. Grohmann and D. Hechtfischer, Cryogenics **17**, 579 (1977).

[13]Y. Mizugaki and R. Kashiwa, J. Phys.: Conf. Ser. **97**, 012056 (2008).

[14]Y. Ishisaki, H. Kurabayashi, A. Hoshino, T. Ohashi, T. Yoshino, T. Hagihara, K. Mitsuda, and K. Tanaka, J. Low Temp. Phys. **151**, 131 (2008).

[15]T. Ohyama, T. Minemoto, M. Itoh, and K. Hoshino, IEEE Trans. Magn. **29**, 3583 (1993).

[16]K. Kamiya, B. Warner, and M. DiPirro, Cryogenics **41**, 401 (2001).

[17]M. Hollister, H. McGregor, A. Woodcraft, D. Bintley, M. MacIntosh, and W. Holland, Proc. of SPIE **7020**, 702023 (2008).

[18]L. Gozzelino, A. Agostino, R. Gerbaldo, G. Ghigo, and F. Laviano, Supercond. Sci. Technol. **25**, 115013 (2012).

[19]U. Hishi, R. Fujimoto, T. Kunihisa, S. Takakura, T. Mitsude, K. Kamiya, M. Kotake, A. Hoshino, and K. Shinozakil, J. Low Temp. Phys. **176**, 1075 (2014).

[20]F. Gomory, M. Solovyov, and J. Souc, Supercond. Sci. Technol. **28**, 044001 (2015).

[21]A. Mager, IEEE Trans. Magn. **6**, 67 (1970).

[22]B. Vasil'ev, V. Ignatovich, and E. Kolycheva, Sov. Phys. Tech. Phys. **23**, 1100 (1978).

[23]J. R. Claycomb and J. H. Miller, Rev. Sci. Instrum. **70**, 4562 (1999).

[24]C. P. Poole, H. A. Farach, R. J. Creswick, and R. Prozorov, *Superconductivity* (Academic Press, London, UK, 2007).

[25]R. Ackermann, F. Wiekhorst, A. Beck, D. Gutkelch, F. Ruede, A. Schnabel, U. Steinhoff, D. Drung, J. Beyer, C. ABmann, L. Trahms, H. Koch, T. Schurig, R. Fischer, M. Bader, H. Ogata, and H. Kado, IEEE Trans. Appl. Supercond. **17**, 827 (2007).

[26]J. Mester, J. M. Lockhart, B. Muhlfelder, D. Murray, and M. Taber, Adv. Space Res. **25**, 1185 (2000).

[27]B. Cabrera and F. van Kann, Acta Astronaut. **5**, 125 (1978).

[28]Q. Geng, H. Minami, K. Chihara, J. Yuyama, and E. Goto, J. Appl. Phys. **72**, 2411 (1992).

[29]R. Clem, IEEE Trans. Magn. **19**, 1278 (1983).

[30]B. xin Xu and W. O. Hamilton, Rev. Sci. Instrum. **58**, 311 (1987).

[31]M. Taber, D. Murray, J. Lockhart, D. Frank, and D. Donegan, Adv. Cryog. Eng. **39(A)**, 161 (1994).

[32]M. M. Fang, J. R. Clem, and D. K. Finnemore, IEEE Trans. Magn. **MAG-23**, 1196 (1987).

[33]J. Ferreirinho and D. Blair, Cryogenics **19**, 702 (1979).

[34]Registered trademark of Vacuumschmelze GmbH & Co. KG.

[35]https://www.comsol.com.

[36]R. M. Bozorth, *Ferromagnetism* (Wiley-IEEE Press, Piscataway, NJ, 1993), Vol. 10.

[37]R. Pecher, M. McCulloch, S. Chapman, L. Prigozhin, and C. Elliott, in Proceedings of the 6th European Conference on Applied Superconductivity EUCAS, Sorrento, Italy, 14-18 September 2003.

[38]F. Grilli, R. Brambilla, and L. Martini, IEEE Trans. Appl. Supercond. **17**, 3155 (2007).

[39]W. M. Roach, D. B. Beringer, Z. Li, C. Clavero, and R. A. Lukaszew, IEEE Trans. Appl. Supercond. **23**, 8600203 (2013).

[40]T. O. M. Itoh, T. Minemoto, K. Numata, and K. Hoshinol, Phys. D: Appl. Phys. **25**, 1630 (1992).

[41]J. Wang and M. Sayerl, IEEE Trans. Appl. Supercond. **3**, 185 (1993).

[42]J. Karthikeyan, A. Paithankar, R. Prasad, and N. C. Son, Supercond. Sci. Technol. **7**, 949 (1994).

[43]T. Cavallin, R. Quarantiello, A. Matrone, and G. Giunchi, J. Phys.: Conf. Ser. **43**, 1015 (2006).

[44]F. Fagnard, S. Elschner, A. Hobl., J. Bock, B. Vanderheyden, and P. Vanderbemden, Supercond. Sci. Technol. **25**, 104006 (2012).

[45]P. Kneisel, G. Ciovati, J. Sekutowicz, A. Matheisen, X. Singer, and W. Singer, in *Particle Accelerator Conference, 2007. PAC.* (IEEE, 2007), pp. 2484–2486.

[46]F. Pobell, *Matter and Methods At Low Temperatures*, 3rd ed. (Springer-Verlag Berlin Heidelberg, 2007).

[47]E. Ramsden, *Hall-effect Sensors: Theory and Application* (Newnes, 2006).

[48]M. Tinkham, *Introduction to Superconductivity* (McGraw-Hill International Editions Signapore, 1996).

[49]C. P. Bean, Rev. Mod. Phys. **36**, 31 (1964).

[50]S. Denis, L. Dusoulier, M. Dirickx, P. Vanderbemden, R. Cloots, M. Ausloos, and B. Vanderheyden, Supercond. Sci. Technol. **20**, 192 (2007).

[51]L. L. VantHull and J. E. Mercereau, Rev. Sci. Instrum. **34**, 1238 (1963).

[52]Y. Xiao, W. Bencze, and D. Hipkins, Czech. J. Phys. **46**, 2873 (1996).